


Polarons and electrical leakage in BaZrO<sub>3</sub> and BaCeO<sub>3</sub>Andrew J. E. Rowberg<sup>1,\*</sup>, Meng Li<sup>2</sup>, Tadashi Ogitsu<sup>1</sup>, and Joel B. Varley<sup>1,†</sup><sup>1</sup>*Quantum Simulations Group and Laboratory for Energy Applications for the Future (LEAF), Lawrence Livermore National Laboratory, Livermore, California 94550, USA*<sup>2</sup>*Energy and Environmental Science and Technology, Idaho National Laboratory, Idaho Falls, Idaho 83415, USA* (Received 2 November 2022; revised 3 January 2023; accepted 10 January 2023; published 25 January 2023)

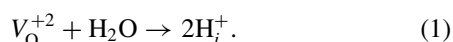
The proton conductors barium zirconate (BaZrO<sub>3</sub>, or BZO), barium cerate (BaCeO<sub>3</sub>, or BCO), and their alloys have attracted considerable interest as solid-state electrolytes in solid-oxide fuel and electrolysis cells. However, the reasons for their non-negligible electrical conductivity, which can limit their performance, are not fully understood. To address that question, we use first-principles calculations based on density functional theory to study the properties of hole and electron polarons in BZO and BCO. We confirm that hole polarons form in both materials, slightly more favorably in BCO. Electron polarons, on the other hand, are stable only in BCO and in Ce-containing alloys; in pure BZO, electron polaron states are unfavorable relative to free carriers, though they become accessible when Ce impurities are introduced. In general, doped BZO and BCO will have negligible electron concentrations, but larger concentrations of holes and hole polarons may be present. Avoiding extreme O-rich conditions and limiting dopant concentrations are key strategies for reducing significant *p*-type electrical leakage. Our results provide physical insights into the different electronic behaviors of BZO and BCO, which can be used to optimize their performance as pure ionic conductors.

DOI: [10.1103/PhysRevMaterials.7.015402](https://doi.org/10.1103/PhysRevMaterials.7.015402)

## I. INTRODUCTION

Proton-conducting oxides (PCOs) are among the best solid-state conductors of hydrogen, making them attractive electrolyte materials in ceramic fuel and/or electrolysis cells [1–4]. Many PCOs have perovskite crystal structures and chemical formulas that can be expressed as ABO<sub>3</sub>, where *A* and *B* are distinct cations. Among these, barium zirconate (BaZrO<sub>3</sub>, hereafter referred to as BZO) and barium cerate (BaCeO<sub>3</sub>, or BCO) are among the most studied, with BZO offering superior chemical stability and BCO having the highest conductivity [5,6]. Both BZO and BCO exhibit nearly pure ionic conductivity, largely on account of their wide band gaps, which is an important feature of an electrolyte.

It is generally proposed that protons (H<sub>i</sub><sup>+</sup>) are introduced into PCOs via the reaction [1]



This expression implies that BZO and BCO must contain high concentrations of oxygen vacancies ( $V_{\text{O}}^{+2}$ ) during operation in order to be protonated upon water exposure. To this end, BZO and BCO are typically doped with elements such as Y, which substitutes on the *B*-site as Y<sub>Zr</sub><sup>-</sup> or Y<sub>Ce</sub><sup>-</sup> [1]. Such acceptor doping will shift the position of the Fermi level closer to the valence-band maximum (VBM), which lowers the formation energy and correspondingly raises the concentration of  $V_{\text{O}}^{+2}$  [7].

BZO and BCO are often alloyed together in devices, yielding an optimal combination of high conductivity and high stability [8–12]. Several studies have shown that these alloys prefer the cubic structure of BZO over the orthorhombic structure of BCO, even at low Zr contents [12–16]. Pure BCO adopts the cubic phase at temperatures exceeding 1223 K [17], but alloys can maintain the cubic structure at much lower temperatures. It has been suggested by some that the cubic structure may contribute to the improved chemical stability of the alloys (relative to BCO) with respect to carbon impurities [18], though other chemical factors are probably more important [19].

BZO and BCO also exhibit different degrees of electrical leakage during device operation. Both materials exhibit almost-pure ionic conduction, although at elevated temperatures, the fraction of electrical conductivity rises noticeably [20]. In both materials, the conductivity of electrons is extremely low ( $<10^{-10}$  S cm<sup>-1</sup>) [21–23], though the conductivity of holes can be sizable at certain conditions, including high partial pressures of O<sub>2</sub> and H<sub>2</sub>O [16,21,24–26]. In general, hole conductivities have been reported to be higher in BZO than in BCO [3,21,27].

The degree of electrical conductivity may be related to the formation of hole polarons, which have been characterized computationally both in BCO [28] and in BZO [29]. Their formation may be stimulated by acceptor doping in these materials, which shifts the Fermi level toward the VBM, where holes form more favorably. Hole polarons form on O sites in these and other oxides, while electron polarons are expected to form on *B*-site cations (Zr and Ce) and have only been calculated for BCO [28,30]. It is distinctly possible that electron polarons cannot form in BZO due to the unfavorability of

\*rowberg1@llnl.gov

†varley2@llnl.gov

oxidizing Zr: in previous computational studies of Zr-doped  $\text{Fe}_2\text{O}_3$  [31] and  $\text{TiO}_2$  [32], it was shown that electrons preferred to localize on Fe or Ti sites rather than Zr sites; on the other hand, extra electrons localized directly on other, more readily reducible, dopant species (e.g., V, Sn, Sb).

In this work, we use computational tools to characterize polaron formation in BZO and BCO. We use density functional theory (DFT) with a hybrid functional, which is necessary to capture the electronic properties of semiconductors and insulators accurately. To begin, we calculate the binding energies of hole and electron polarons in BZO and BCO, considering both the metastable cubic phase of BCO as well as its preferred orthorhombic phase, as cubic BCO can be considered to be the Ce-pure endpoint of cubic BZO–BCO alloys. Our results are in good agreement with previous calculations of polarons for orthorhombic BCO [28,30] and cubic BZO [29]. We show definitively that electron polarons cannot form in BZO, as they have a large, negative binding energy of  $-0.95$  eV, meaning that electrons will simply populate conduction band states. Furthermore, we expand upon previous work by calculating polarons in the presence of alloy impurities, thereby building a picture of polaron formation in alloys of BZO and BCO. By considering the absolute band alignment of BZO and BCO in conjunction with calculations in model alloy structures, we show schematically how polaron binding energies vary across the materials. Our results suggest Zr sites exhibit a slight preference for hole polaron formation, which becomes stronger in the limit of higher Ce contents.

Based on defect formation energies of dopants and native point defects, along with carrier concentrations determined by integrating the density of states (DOS), we calculate the concentrations of relevant species and the Fermi level positions as a function of O chemical potential. In doing so, we identify extreme O-rich conditions, corresponding to Fermi levels close to the VBM, as being most likely to lead to electrical leakage, due to the high resultant concentrations of holes. In BCO and Ce-rich alloys, the preferability of polaron formation coupled with their lower mobility likely contributes to the lower hole conductivities reported in previous studies. Our results provide physical insights into some of the sources contributing to electrical leakage in BZO and BCO and their alloys, which must be carefully taken into account in order to optimize the performance of these materials as pure ion-conducting PCOs.

## II. COMPUTATIONAL METHODS

We perform DFT calculations [33,34] as implemented in the Vienna *Ab initio* Simulation Package (VASP) [35]. In order to obtain accurate results for electronic properties, we use the hybrid exchange-correlation functional of Heyd, Scuseria, and Ernzerhof (HSE06) [36], which provides superior accuracy for electronic properties compared to approaches based on the generalized gradient approximation (GGA). We use a mixing parameter of  $\alpha = 0.25$  (representing the amount of exact Hartree-Fock exchange used) for all calculations, except where otherwise stated. While our hybrid DFT approach does not perfectly describe  $f$  electrons, as are present in Ce, we justify its use in that it yields excellent agreement with experimental results for both structural and electronic

properties of BCO. Furthermore, we neglect the effect of spin-orbit coupling, as it has previously been found to make a negligible difference in the electronic properties of BCO [37]. We apply projector augmented wave (PAW) potentials [38,39] with a plane-wave cutoff of 500 eV. The Ba  $5s^2 5p^6 6s^2$ , Sr  $4s^2 4p^6 5s^2$ , Zr  $4s^2 4p^6 5s^2 4d^2$ , Ce  $5s^2 5p^6 6s^2 5d^1 4f^1$ , and O  $2s^2 2p^4$  electrons are treated explicitly as valence. For orthorhombic unit cells, each containing four formula units, a  $4 \times 4 \times 3$   $k$ -point grid is used to integrate over the Brillouin zone, while for cubic unit cells, containing one formula unit, an  $8 \times 8 \times 8$   $k$ -point grid is used. We use finer  $k$ -point meshes to calculate the DOS,  $10 \times 10 \times 8$  for orthorhombic BCO and  $16 \times 16 \times 16$  for BZO. For polaron and defect calculations, we construct  $3 \times 3 \times 3$  supercells for BZO and cubic BCO, containing 135 atoms, and a  $2 \times 2 \times 2$  supercell for orthorhombic BCO, containing 160 atoms. When defects are added, we explicitly break the symmetry of the cell, and all atoms are allowed to relax. For supercell and slab calculations, a single special  $k$  point is used. Spin polarization is used for all calculations.

### A. Defect formation and concentrations

We calculate formation energies using the standard approach for point defects [45]:

$$E^f(D^q) = E_{\text{tot}}(D^q) - E_{\text{bulk}} + \sum n_A \mu_A + qE_F + \Delta_{\text{corr}}. \quad (2)$$

$E_{\text{tot}}(D^q)$  is the total energy of a supercell containing defect  $D^q$ ;  $E_{\text{bulk}}$  is the total energy of the same supercell containing no defects;  $n_A$  is the number of atoms of species A added ( $n_A < 0$ ) or removed ( $n_A > 0$ ) from the system to create the defect;  $\mu_A$  is the chemical potential of A;  $E_F$  is the position of the Fermi level; and  $\Delta_{\text{corr}}$  is a finite-size correction term for charged defects [46,47]. To determine these corrections, we use our calculated low-frequency dielectric constants of 57.25 for  $\text{BaZrO}_3$  and 98 for  $\text{BaCeO}_3$ . The formation energy determines the concentration of defects  $c$  via a Boltzmann relation

$$c = N_{\text{sites}} \exp\left(-\frac{E^f}{k_B T}\right). \quad (3)$$

Once the formation energies have been computed, the position of the Fermi level can be determined by charge neutrality, i.e., where there are equal concentrations of positively and negatively charged defects.

The chemical potentials  $\Delta\mu_A$  are referenced to the energy of A in its bulk energetic ground state. For Ba, Zr, and Ce, these are elemental solids, while for O, the ground state is molecular  $\text{O}_2$ . The values of  $\Delta\mu_O$  can be connected to experimentally measurable partial pressures of  $\text{O}_2$  using the expression

$$\Delta\mu_A = H^0(T) - TS^0(T) + RT \ln \frac{p_A}{p^0}, \quad (4)$$

where  $H^0(T)$  and  $S^0(T)$  are tabulated for gases like  $\text{O}_2$ ,  $p_A$  is the partial pressure, and  $p^0$  is the pressure at the standard conditions used in the tabulation [48].

In addition to defect concentrations, we can also determine concentrations of free carriers (i.e., electrons and holes) as a function of Fermi level. We determine electron concentrations

TABLE I. Calculated and experimental bulk properties for BaZrO<sub>3</sub> and BaCeO<sub>3</sub> in cubic and orthorhombic unit cells. Structural properties and enthalpy of formation as expressed per formula unit (“per f.u.”).

| Compound           | Unit cell    | Method | $a$ (Å)           | $b$ (Å)           | $c$ (Å)           | Volume (Å <sup>3</sup> /f.u.) | $\Delta H^f$ (eV/f.u.) | $E_g^{\text{dir}}$ (eV) | $E_g^{\text{ind}}$ (eV) |
|--------------------|--------------|--------|-------------------|-------------------|-------------------|-------------------------------|------------------------|-------------------------|-------------------------|
| BaZrO <sub>3</sub> | Cubic        | HSE    | 4.20              |                   |                   | 74.12                         | -17.29                 | 4.97                    | 4.69                    |
|                    |              | Expt   | 4.20 <sup>a</sup> |                   |                   | 74.09                         | -18.28 <sup>b</sup>    | 5.0 <sup>c</sup>        |                         |
| BaCeO <sub>3</sub> | Orthorhombic | HSE    | 6.23              | 6.23              | 8.78              | 85.09                         | -16.89                 | 4.15                    | 4.15                    |
|                    |              | Expt   | 6.23 <sup>d</sup> | 6.24 <sup>d</sup> | 8.82 <sup>d</sup> | 85.74                         | -17.52 <sup>e</sup>    | 4.1 <sup>f</sup>        |                         |
|                    | Cubic        | HSE    | 4.43              |                   |                   | 86.86                         | 16.71                  | 4.44                    | 4.20                    |
|                    |              | Expt   | 4.45 <sup>d</sup> |                   |                   | 87.82                         |                        |                         |                         |

<sup>a</sup>Reference [40]; <sup>b</sup>Reference [41]; <sup>c</sup>Reference [42]; <sup>d</sup>Reference [17]; <sup>e</sup>Reference [43]; <sup>f</sup>Reference [44].

by integrating the calculated DOS near the conduction band minimum (CBM), using the expression [49]

$$n = \int_{E_{\text{CBM}}}^{\infty} g_{\text{C}}(E)f(E)dE \quad (5)$$

with  $g_{\text{C}}(E)$  being the conduction band DOS and  $f(E)$  being the Fermi-Dirac occupation function. Similarly, for holes, we determine the carrier concentration via

$$p = \int_{-\infty}^{E_{\text{VBM}}} g_{\text{V}}(E)[1 - f(E)]dE, \quad (6)$$

with  $g_{\text{V}}(E)$  being the valence band DOS.

### B. Polaron calculations

We calculate polarons in supercells by changing the number of electrons and perturbing the atomic environments to prompt charge localization. For a hole polaron, an electron is removed, and Zr/Ce–O bonds are extended around one O atom; for an electron polaron, an electron is added, and Zr/Ce–O bonds are extended around one Zr/Ce atom.

Once the polarons have been stabilized, we calculate their polaron binding energies, which quantify the energetic preference for a free carrier to form a polaron. The binding energy is related to the hypothetical formation energy of the polaron, which we calculate using Eq. (2). Note that formation energies for polarons do not depend on the chemical potential, as  $n_{\text{A}} = 0$ . For hole polarons, the binding energy is simply the negative of their formation energy at  $E_{\text{F}} = 0$  eV (i.e., at the VBM), while for electron polarons, the binding energy is the negative of their formation energy at  $E_{\text{F}} = E_{\text{g}}$  (i.e., at the CBM). As the polarons have charge  $q = \pm 1$ , these quantities are equivalent to the distance from the VBM or CBM at which the polaron formation energy becomes positive. If the binding energy is positive, the polaron can form in the material, and the more positive the energy, the greater the stability of polarons relative to delocalized carriers.

Additionally, we estimate the polaron migration barriers by linearly interpolating between initial and final configurations and calculating the energies of intermediate states, without allowing for structural relaxation.

## III. RESULTS

### A. Bulk properties

We begin with our calculations of the bulk lattice constants, enthalpies of formation, and band gaps, summarized

in Table I, for cubic BZO and for BCO in both its cubic and orthorhombic unit cells. Our results compare well with experimental data where available. The band gap of cubic BCO has not been measured experimentally, and one previous computational study reports a much smaller value (2.17 eV) than we do [50]; however, this discrepancy is likely due to their use of the GGA level of theory, which is known to underestimate band gaps.

We plot the band structures for all three compounds, alongside their DOS, in Fig. 1. In all three compounds, the VBM is comprised predominantly of O  $2p$  states; however, the CBM states differ, with Zr  $d$  states comprising the CBM of BZO and Ce  $f$  states doing the same for BCO. The Ce  $f$  bands have less dispersion than do bands comprised of  $d$  states, giving rise to a flatter CBM in BCO than in BZO. In BCO’s orthorhombic unit cell, these  $f$  states are separated by approximately 0.5 eV from the next-lowest conduction bands, which are primarily composed of Ce  $d$  states and look qualitatively similar to the Zr  $d$  CBM states of BZO. In cubic BCO, however, the Ce  $f$  states overlap with the higher-lying  $d$ -state bands.

We summarize the effective masses for electrons ( $m_e^*$ ) and holes ( $m_h^*$ ) extracted from our band structures in Table II. In general, our results show lower  $m_h^*$  and  $m_e^*$  in BZO as compared to BCO. For  $m_h^*$ , we include values for the three highest valence bands (VB1, VB2, and VB3), which are nearly degenerate at the VBM for the cubic structures; however, the VBM in orthorhombic BCO is nondegenerate and, as such, we only considered the highest valence band. As shown in Table II, the hole effective masses are relatively large and anisotropic. When considering these large effective masses alongside the electronic and ionic dielectric constants in both BZO and BCO, we can estimate hole polaron Fröhlich coupling constants [51] on the order of 3 and 4, respectively, assuming an effective optical phonon frequency of  $\sim 700$  cm<sup>-1</sup>, which is in line with tabulated data from the Materials Project [52]. These values strongly suggest that polaronic distortions mediate hole transport in these materials. For electrons, the estimated coupling constants are low for BZO (1.1) and much higher for BCO (3.9), again suggesting a tendency for electron polaron formation in BCO. In the following sections we show how carrier trapping is indeed favorable in these materials and consistent with this suggested behavior.

### B. Polarons

#### 1. Bulk polarons

We proceed in our investigation by calculating polarons in BZO and BCO. As polarons have previously been calculated

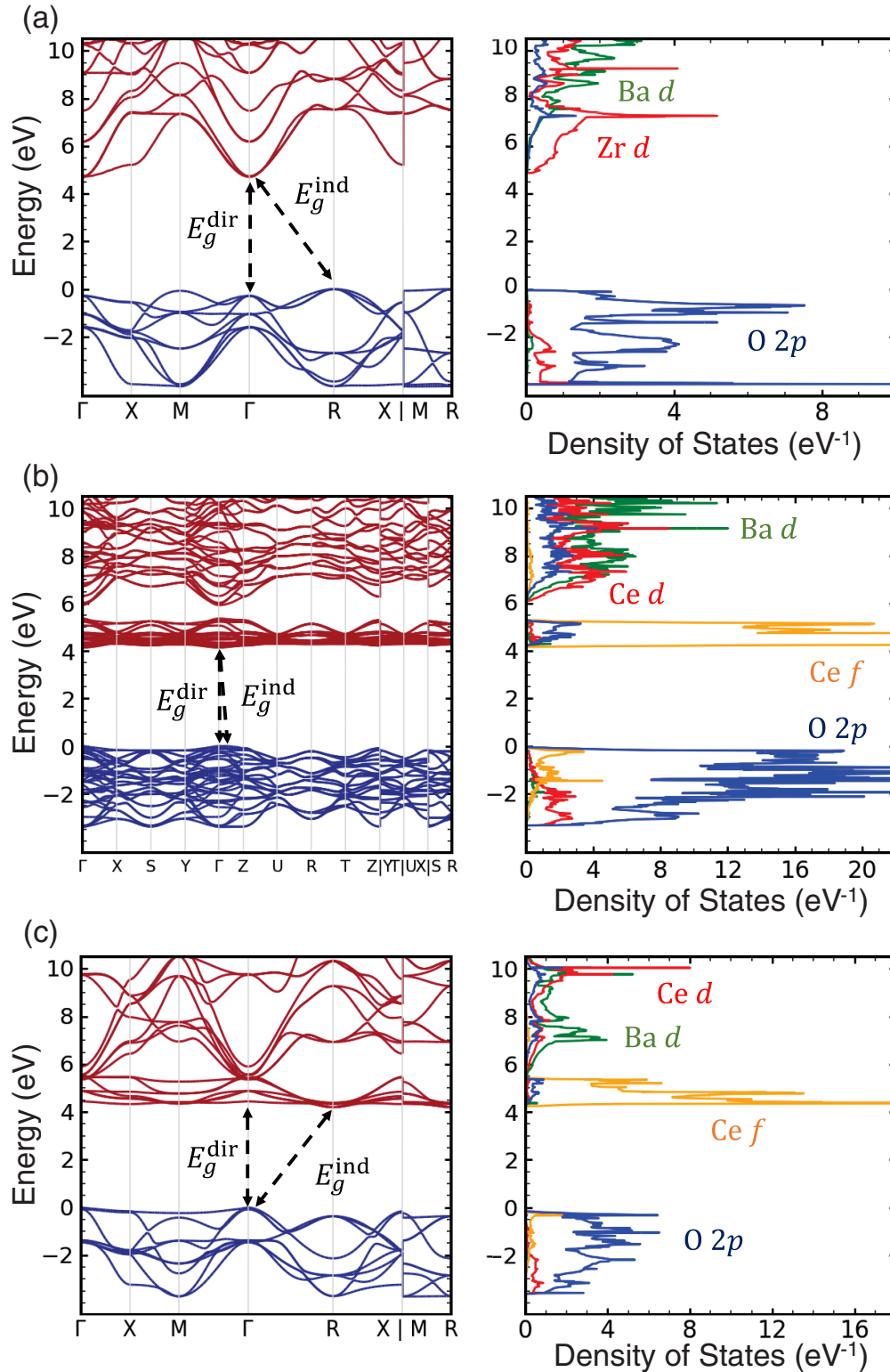


FIG. 1. Band structures and densities of states (DOS) for (a) cubic BaZrO<sub>3</sub>, (b) orthorhombic BaCeO<sub>3</sub>, and (c) cubic BaCeO<sub>3</sub>. Direct ( $E_g^{\text{dir}}$ ) and indirect ( $E_g^{\text{ind}}$ ) band gaps, listed in Table I, are labeled in the band structures.

in orthorhombic BCO, we begin there. Similarly to Swift *et al.* [28], we find that both hole and electron polarons can form readily. Their geometries are shown in Figs. 2(a) and 2(b). Hole polarons preferentially localize on an apical O

atom bridging two Ce atoms along the  $c$  axis, and they stretch neighboring Ce–O bonds by 7.1%–7.3%. Hole polarons on the crystallographically distinct planar O site are 55 meV higher in energy, indicating a slight preference for localization

TABLE II. Effective masses for holes and electrons (in units of the electron mass  $m_0$ ) evaluated in the vicinity of the valence and conduction band extrema, respectively. For the VBM, this at R in BZO, slightly off  $\Gamma$  in orthorhombic BCO ( $\Gamma^*$ ), and at  $\Gamma$  in cubic BCO.

| Material                 | Direction                       | VB1 $m_h^*$ ( $m_0$ ) | VB2 $m_h^*$ ( $m_0$ ) | VB3 $m_h^*$ ( $m_0$ ) | Direction                | $m_e^*$ ( $m_0$ ) |
|--------------------------|---------------------------------|-----------------------|-----------------------|-----------------------|--------------------------|-------------------|
| BaZrO <sub>3</sub>       | R $\rightarrow$ $\Gamma$        | 0.96                  | 0.43                  | 0.43                  | $\Gamma \rightarrow$ X   | 0.26              |
|                          | R $\rightarrow$ X               | 1.18                  | 0.48                  | 0.36                  | $\Gamma \rightarrow$ M   | 0.25              |
|                          | R $\rightarrow$ M               | 2.68                  | 0.19                  | 0.19                  | $\Gamma \rightarrow$ R   | 0.20              |
| Ortho BaCeO <sub>3</sub> | $\Gamma^* \rightarrow$ $\Gamma$ | 5.03                  |                       |                       | $\Gamma \rightarrow$ X   | 2.94              |
|                          | $\Gamma^* \rightarrow$ Z        | 1.05                  |                       |                       | $\Gamma \rightarrow$ Y   | 2.87              |
|                          |                                 |                       |                       |                       | $\Gamma \rightarrow$ Z   | 3.54              |
| Cubic BaCeO <sub>3</sub> | $\Gamma \rightarrow$ X          | 0.38                  | 1.82                  | 0.18                  | R $\rightarrow$ $\Gamma$ | 0.93              |
|                          | $\Gamma \rightarrow$ M          | 0.40                  | 0.47                  | 0.24                  | R $\rightarrow$ X        | 1.10              |
|                          | $\Gamma \rightarrow$ R          | 0.36                  | 0.34                  | 0.34                  | R $\rightarrow$ M        | 1.09              |

on the apical O atoms. By inspection, hole polarons have the same O  $2p$  character as the VBM. Similarly, electron polarons derive from the Ce  $4f$  states of the CBM, localizing on a single Ce atom and extending neighboring Ce–O bonds by 4.9%–5.3%. We compute polaron binding energies of 0.11 eV for hole polarons and 0.74 eV for electron polarons. We estimate a migration barrier of 0.17 eV for hole polarons to move between the apical and planar sites (0.11 eV for the reverse movement). For electron polarons, the migration barrier ranges from 0.29–0.33 eV depending on the direction.

For cubic BZO, we localize the hole polaron on one O atom [Fig. 2(c)], with O  $2p$  lobes perpendicular to the Zr–O bond, in similar fashion to orthorhombic BCO. The two Zr–O bonds coordinated with the polaron are 4.8% longer than in bulk BZO. We calculate the hole polaron binding energy to be 0.08 eV. Thus, overall, our results suggest that holes exhibit similar polaronic binding strengths of 0.11 and 0.08 eV in pure BCO and BZO, respectively. We estimate its migration barrier to be 0.08 eV, which is roughly 1.5–2 $\times$  smaller than the barrier for hole polarons in BCO.

However, in BZO, the electron polaron state cannot be localized using the same computational approach as with BCO. Rather than localizing on a perturbed Zr atom, an extra electron added to the system will be resonant with the CBM. We confirm this finding with multiple approaches, including the polaron self-interaction correction (pSIC) approach [54] and the use of a larger supercell for BZO.

One other option we explore to stabilize the electron polaron involves changing the value of the HSE mixing parameter  $\alpha$ . Increasing  $\alpha$  increases the band gap by shifting the CBM higher in energy and the VBM lower in energy; thus, it may be possible to separate the polaron state from the conduction bands at high enough values of  $\alpha$ . Indeed, we find that  $\alpha = 0.6$  is sufficient to allow the electron polaron to localize on a Zr  $d$  state, as shown in Fig. 2(d). Due to the symmetry of  $d$  states, these polarons extend four of the neighboring Zr–O bonds markedly more than the other two; for  $\alpha = 0.6$ , the four longest bonds are extended by 3.8%, and the shorter two are extended by 1.1%.

As shown in Fig. 3, the binding energy associated with the polaron state (referenced to the CBM position in the figure) varies linearly with  $\alpha$  over the range of values associated with a localized polaron state; the same is true of the VBM and CBM positions. Therefore, we extrapolate the polaron binding energy for  $\alpha = 0.25$  by extending a linear fit to the data for

$\alpha \geq 0.6$ . In this way, we find the polaron binding energy to be  $-0.95$  eV for  $\alpha = 0.25$ .

Describing polarons in cubic BCO is not straightforward, given that the structure is dynamically unstable. Introducing any distortions that break the cubic symmetry prompt a relaxation toward the stable orthorhombic crystal structure, meaning that Ce–O<sub>6</sub> octahedra are distorted throughout the supercell. In particular, our attempts to stabilize hole polarons, which distort only two Ce–O bonds and as such have lower rotational symmetry than the cubic structure, cause significant distortion in the structure. As such, we do not claim that our calculations of polarons in the cubic BCO system are quantitatively meaningful, although these results do highlight the strong interplay between local distortions and polaronic localization, particularly with holes. Such effects are expected to be more pronounced in alloys or doped phases that exhibit a wider variation of local atomic environments that may foster carrier trapping.

Electron polarons are perhaps most meaningful in this context, as they do not disrupt the cubic symmetry of the supercell. The electron polaron in cubic BCO localizes on Ce  $4f$  states, much like in orthorhombic BCO, and it extends the six nearby Ce–O bonds by 4.1%. We estimate a binding energy of 0.64 eV and a migration barrier of 0.25 eV, both of which values are slightly less than those in the orthorhombic phase.

## 2. Polarons in BZO–BCO alloys

Polarons may interact with impurities, including alloy species where Ce substitutes for Zr in BZO ( $\text{Ce}_{\text{Zr}}$ ) or Zr substitutes for Ce in BCO ( $\text{Zr}_{\text{Ce}}$ ). We calculate these polaronic states in much the same fashion as bulk polarons, i.e., by introducing some amount of atomic distortion and adding or removing charge, starting from the relaxed neutral configuration of the supercell containing a single alloy species ( $\text{Ce}_{\text{Zr}}^0$  or  $\text{Zr}_{\text{Ce}}^0$ ). In order to calculate the polaron binding energies, we again use Eq. (2), but rather than referencing the formation energy to the bulk supercell, we reference it to the total energy of a supercell containing a single  $\text{Ce}_{\text{Zr}}^0$  or  $\text{Zr}_{\text{Ce}}^0$  (i.e.,  $E_{\text{bulk}} = E_{\text{tot}}[\text{Ce}_{\text{Zr}}^0]$  for BZO, and  $E_{\text{bulk}} = E_{\text{tot}}[\text{Zr}_{\text{Ce}}^0]$  for BCO). We note that, in cubic BCO, introducing such states disrupts the dynamically unstable structure; as such, we do not consider polaronic alloy states in cubic BCO.

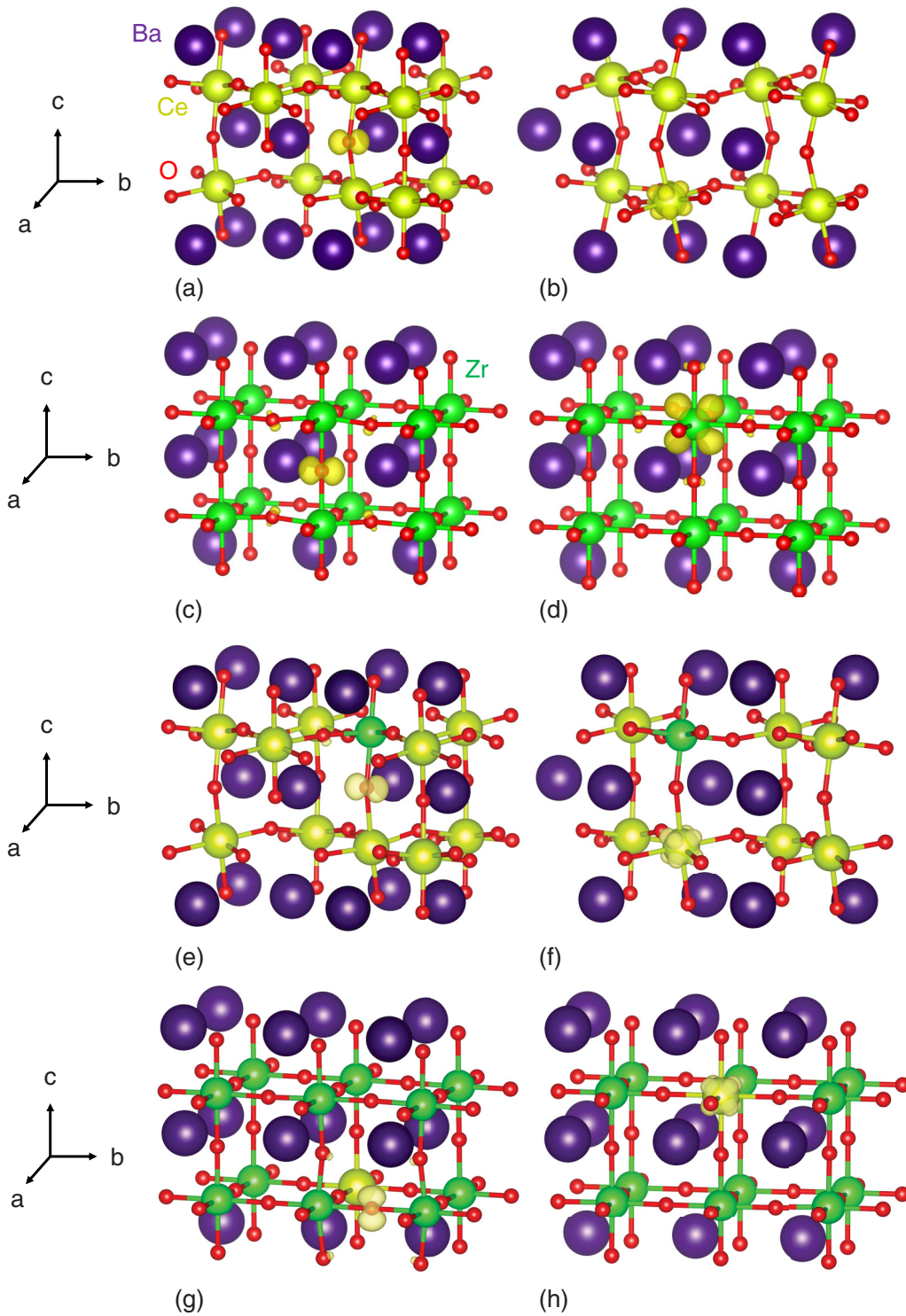


FIG. 2. Structural representations of polarons in BCO and BZO. For orthorhombic BCO, the lowest-energy hole polaron is shown in (a), and the electron polaron is shown in (b). For cubic BZO, the hole polaron is shown in (c), and the electron polaron (using an HSE mixing parameter of  $\alpha = 0.9$ ) is shown in (d). Polaronic alloy states are also shown: for orthorhombic BCO,  $\text{Zr}_{\text{Ce}}^+$  in (e) and  $\text{Zr}_{\text{Ce}}^-$  in (f); for BZO,  $\text{Ce}_{\text{Zr}}^+$  in (g) and  $\text{Ce}_{\text{Zr}}^-$  in (h). All images are generated using the VESTA 3 software [53].

We begin our discussion with  $\text{Zr}_{\text{Ce}}$  in orthorhombic BCO, which is representative of the dilute alloy phase of BCO:Zr. The hole polaron configuration  $\text{Zr}_{\text{Ce}}^+$  is shown in Fig. 2(e). It looks nearly identical to the bulk hole polaron, with

the localized O  $2p$  state lying between one Ce atom and the Zr impurity atom. Compared to bond lengths for  $\text{Zr}_{\text{Ce}}^0$ , the Zr–O bond length increases by 5.1%, and the Ce–O bond length increases by 8.4%. We calculate a hole polaron binding

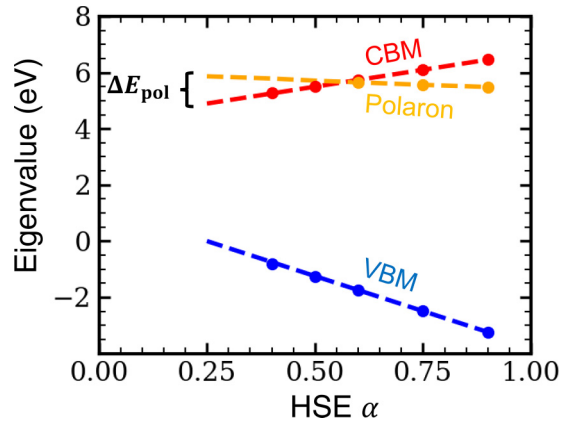


FIG. 3. Extrapolation of the position of the electron polaron binding energy in BZO, obtained by varying the HSE mixing parameter  $\alpha$ , and using linear interpolation to track the change of the eigenvalues associated with the VBM and CBM, and the polaron binding energies. Eigenvalues are referenced to the value corresponding to the VBM in the spin channel containing the polaron state, for  $\alpha = 0.25$ .  $\Delta E_{\text{pol}}$ , labeled in the figure, is the electron polaron binding energy for  $\alpha = 0.25$ .

energy of 0.31 eV for this species. The electron polaron configuration  $\text{Zr}_{\text{Ce}}^-$  is seen in Fig. 2(f). Notably, the Zr atom does not host the polaron, which instead resides on the 4*f* states of a nearby Ce atom. This situation matches that observed in materials like Fe<sub>2</sub>O<sub>3</sub> and TiO<sub>2</sub>, where the native cations are more readily reduced than Zr impurities [31,32]. The Ce–O bonds neighboring the polaron extend by 4.3%–5.4% relative to the equivalent bonds in the  $\text{Zr}_{\text{Ce}}^0$  supercell, which matches the effect of the electron polaron in bulk BCO. We calculate a binding energy of 0.80 eV for this electron polaron. Our calculations suggest that BCO:Zr leads to a more pronounced stabilization of hole polarons, with binding energies of 0.31 eV compared to 0.11 eV in pure BCO, while electron polarons are more modestly stabilized (increase of 0.06 eV in the polaron binding energy).

Next, we discuss  $\text{Ce}_{\text{Zr}}$  in BZO, representative of the dilute alloy BZO:Ce. We show the hole polaron configuration  $\text{Ce}_{\text{Zr}}^+$  in Fig. 2(g). The energetically preferred configuration sees the hole polaron lie between two Zr atoms, with the Ce atom further away. We calculate the hole polaron binding energy to be 0.12 eV. Coupled with our result for BCO showing hole polarons to prefer being close to the Zr impurity atom, this finding implies that Zr provides a nucleation site of sorts for hole polarons. The two Zr–O bonds around the polaron increase in length by 5.0%, almost identical to the hole polaron in bulk BZO. Conversely, the electron polaron configuration  $\text{Ce}_{\text{Zr}}^-$ , shown in Fig. 2(h), sees charge localized on the impurity atom. The Ce–O bond lengths surrounding the polaron increase in length by 3.3%; this bond stretching is smaller than that of the electron polaron in BCO mainly due to the smaller size of BZO’s lattice. Clearly, while electron polarons in bulk BZO cannot be stabilized, the addition of Ce makes them accessible, implying that they may be observed in alloys. We find its binding energy to be 0.61 eV. These results suggest that Ce incorporation into BZO has a modest effect on hole stabilization (polaron binding energies of 0.12 eV vs

0.08 eV in bulk BZO), while electron localization on Ce is expected but weakened relative to that in pure BCO (0.61 eV vs 0.74 eV). Taken together with our results for BCO:Zr, carrier trapping is expected to exhibit an anisotropy with respect to composition, with hole localization preferring environments containing Zr, and electron trapping preferred at Ce sites.

In order to confirm the preferential formation of hole polarons next to Zr atoms, we construct a cubic alloy supercell containing roughly equal amounts of Ce and Zr atoms randomly distributed on the *B* sites and create hole polarons on various sites. The structure contains some intrinsic octahedral distortion, which is primarily limited to the Ce–O<sub>6</sub> octahedra; however, these distortions are minimized by the presence of Zr. Furthermore, unlike in cubic BCO, adding hole polarons does not affect the distortion significantly beyond the neighboring cations. We place hole polarons on O atoms in their three distinct coordination environments: between two Zr atoms (Zr–O–Zr), between two Ce atoms (Ce–O–Ce), and between one Zr atom and one Ce atom (Zr–O–Ce). Polarons are most favored on Zr–O–Zr sites and least favored on Ce–O–Ce sites, by about 0.5 eV on average. Additionally, we estimate polaron migration barriers for one characteristic pathway in the alloy supercell. The barrier between Ce–O–Ce and Zr–O–Ce sites is 0.06 eV (0.30 eV for the reverse movement); subsequently, the barrier between Zr–O–Ce and Zr–O–Zr sites is 0.19 eV (0.53 eV in reverse); this result implies that polarons will be trapped on Zr–O–Zr sites in alloys. However, they can likely move between neighboring Zr–O–Zr sites relatively easily, based on our calculated barrier (0.08 eV) for bulk BZO. Thus, it seems likely that Ce-rich alloys will have a lower hole polaron mobility than Zr-rich alloys.

### C. Band alignments

We next integrate our results for band structures and polaron binding energies to generate a comprehensive picture of relative polaron positions across the three systems under study here. To do so, we compute band offsets by following the established approach of constructing heterostructures, in this case of BZO and both cubic and orthorhombic BCO [55,56]. We specifically follow the procedure described in Ref. [57], whereby the electrostatic potential offset is determined using strained heterostructures calculated at the GGA level of theory for computational efficiency. Coupling these offsets with the HSE band structures (calculated for strained geometries) yields results with very low error relative to an all-HSE approach. In our calculations, we take cubic BZO as the substrate structure, meaning that cubic and orthorhombic BCO structures are strained to BZO’s lattice in the heterostructures.

The band alignment we obtain is shown in Fig. 4, with the positions of the VBM and CBM indicated as black lines for all three systems. Our computed band offsets are indicated in the figure. BZO and orthorhombic BCO exhibit a type I offset, wherein the band extrema of BCO fall within the band gap of BZO; however the positions of the VBMs are very similar (within 0.03 eV), with the CBM offset more significant. BZO and cubic BCO also exhibit a type I offset, although in comparing those two band structures, the positions of the CBM

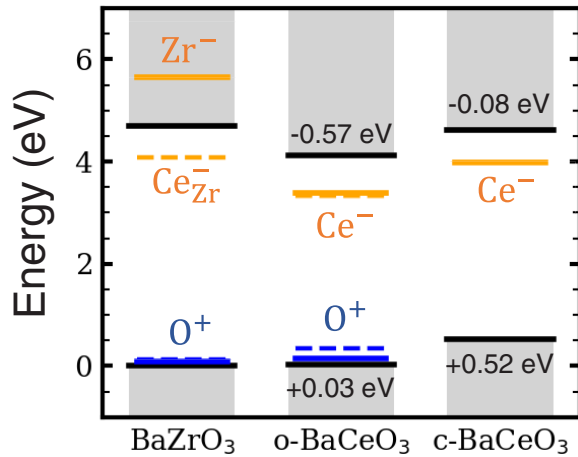


FIG. 4. A band offset diagram showing the absolute alignments for cubic  $\text{BaZrO}_3$ , orthorhombic (“o”)  $\text{BaCeO}_3$ , and cubic (“c”)  $\text{BaCeO}_3$ . Conduction and valence band states are shaded gray. The energy scale is referenced to the VBM of  $\text{BaZrO}_3$ . For  $\text{BaCeO}_3$ , the positions of the VBM and CBM relative to those of  $\text{BaZrO}_3$  are labeled. Polaron levels based on calculated binding energies are also shown, with hole polarons labeled as  $\text{O}^+$  in blue and electron polarons labeled as  $\text{Ce}^-$  or  $\text{Zr}^-$  in orange. Polaron states resulting from alloying are shown with dashed lines; other than  $\text{Ce}_{\text{Zr}}^-$ , these dashed lines are not specifically labeled.

are very close (within 0.08 eV), while the VBMs are further apart.

This result has potential implications in BZO–BCO alloys, which can be approximated from linear interpolations of the parent BCO and BZO end compounds. Considering the cubic phases for BZO–BCO alloys, band transport for holes would preferably be driven to more Ce-rich regions, considering the higher VBM of these materials on an absolute energy scale in Fig. 4. Combined with the propensity for hole trapping by Zr in Ce-rich materials, it is likely that hole conductivities will be lower in Zr-poor BZO–BCO alloy compositions, or phase-segregated regions with lower Zr contents. In terms of electron conductivity, the similar conduction band positions and strong electron trapping by Ce regardless of composition indicate very poor electron mobilities.

We also show the polaron binding energies for each material relative to their respective band extrema (hole polarons  $\text{O}^+$ , and electron polarons  $\text{Zr}^-$ ,  $\text{Ce}^-$ , and  $\text{Ce}_{\text{Zr}}^-$ ). The binding energies for polaronic alloy states are shown with dashed lines. Other than  $\text{Ce}_{\text{Zr}}^-$ , for which the polaronic state is localized on the impurity, we do not label these lines explicitly, as the polaron configurations are almost identical to those of the bulk compounds. We note that, among the three polaronic alloy states that resemble bulk polarons, the binding energy only differs significantly (by more than  $\approx 0.05$  eV) for hole polarons in orthorhombic BCO; this sizable difference may be due to the intrinsic distortion introduced by the neighboring Zr impurity, which makes the hole polaron even more energetically preferable. In general, the polaron positions are roughly equidistant from their band extrema in all three systems, although orthorhombic BCO appears to have the most accessible polaron states based on their relatively high binding energies.

#### D. Defect concentrations and Fermi level positions

Ultimately, the appearance of polarons and free charge carriers will be tied to the processing conditions and Fermi levels in devices. To understand how these factors are intertwined in BZO and BCO, we conduct an analysis based on formation energies [Eq. (2)] and concentrations [Eq. (3)] of defects to examine how the defect and carrier concentrations change as a function of temperature and chemical potential.

We show our results for defect concentrations and resulting equilibrium Fermi levels in Fig. 5. For  $\text{Y}_{\text{Zr}}^-$  and  $\text{Y}_{\text{Ce}}^-$ , we fix the impurity concentration at 20 at.%, corresponding to compositions  $\text{BaZr}_{0.8}\text{Y}_{0.2}\text{O}_3$  and  $\text{BaCe}_{0.8}\text{Y}_{0.2}\text{O}_3$ , respectively, which are among the most heavily doped samples commonly reported in the literature [3]. We assume a fixed temperature of 900 K, which is close to typical operating temperatures for BZO- and BCO-based fuel and electrolysis cells [4,11], and allow the O chemical potential to vary from  $\Delta\mu_{\text{O}} = -4$  to 0 eV. We indicate the partial pressures corresponding to each value of  $\Delta\mu_{\text{O}}$ , determined with Eq. (4), on the upper x axis in Fig. 5. For both BZO and BCO, we show concentrations at intermediate chemical potential conditions, averaging between the Ba-rich and Ba-poor limits identified in previous work [7,28]. We explicitly determine that defect concentrations at the Ba-rich and Ba-poor limits are very similar to those at these intermediate chemical potentials. We use defect formation energies calculated previously [7,28] to generate these plots, supplemented by new calculations here for cation antisite defects ( $\text{Ce}_{\text{Ba}}^{+2}$  and  $\text{Ba}_{\text{Ce}}^{-2}$ ) and  $\text{Y}_{\text{Ba}}^+$  in BCO, for which formation energies had not been calculated in prior work. For  $V_{\text{O}}$ , we apply a finite-temperature correction by accounting for vibrational free-energy effects, using the results of Sundell *et al.* to obtain a modest formation energy increase of 0.13 eV [58]. We apply this same correction to  $V_{\text{O}}$  in BCO.

In BZO [Fig. 5(a)], we see that the defect chemistry will be dominated by  $\text{Y}_{\text{Zr}}^-$  and  $V_{\text{O}}^{+2}$ .  $V_{\text{O}}^{+2}$  maintains the same concentration throughout the range of O chemical potentials shown. Among free carriers, electrons ( $e^-$ ) have negligible concentrations, while holes ( $h^+$ ) are considerably more prevalent, increasing in concentration for more O-rich conditions, though they never surpass  $V_{\text{O}}^{+2}$  as the dominant donor species. This result matches expectations from experiments, which show an increase in hole conductivity as  $\text{O}_2$  partial pressures increase [26].

In BCO [Fig. 5(b)], we again observe  $\text{Y}_{\text{Ce}}^-$  and  $V_{\text{O}}^{+2}$  dominating the defect chemistry for most chemical potential conditions. However,  $\text{Ce}_{\text{Ba}}^{+2}$  antisite donors will also be prevalent. This result is noteworthy, considering that such antisite defects have not been calculated before but clearly are relevant to the defect chemistry. Similarly, “wrong-site” dopant species  $\text{Y}_{\text{Ba}}^+$  have reasonably high concentrations, in contrast to the much higher formation energy of such species in BZO. Again,  $e^-$  concentrations are negligible, and  $h^+$  concentrations are similar to those in BZO.

In addition to tracking changes in defect concentrations, we also observe a monotonic decrease in the Fermi level relative to the VBM with higher oxygen partial pressures (increasing  $\Delta\mu_{\text{O}}$ ), both for BZO and for BCO. Naturally, as the Fermi level approaches the VBM,  $e^-$  concentrations drop, and  $h^+$  concentrations rise. A Fermi level roughly 1 eV above the



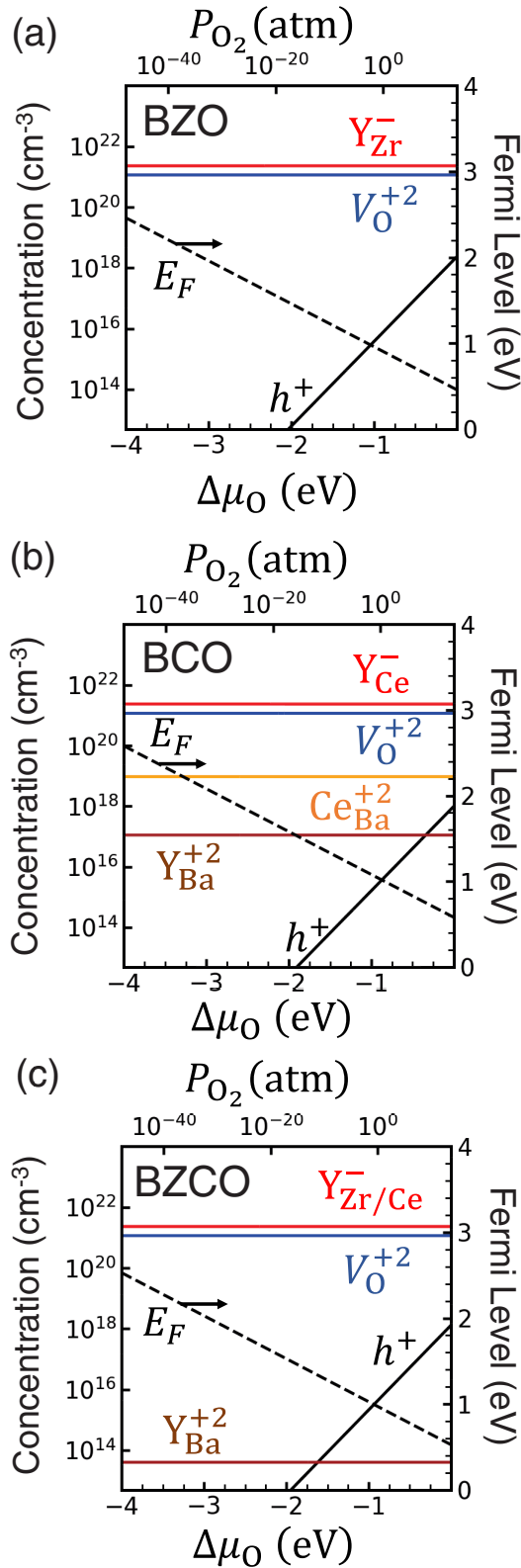


FIG. 5. Defect and carrier concentrations and Fermi level ( $E_F$ ) positions relative to the VBM under intermediate chemical potential conditions in (a) BZO, (b) BCO, and (c) Ba(Zr<sub>0.5</sub>Ce<sub>0.5</sub>)O<sub>3</sub> alloys, for which concentrations are estimated by interpolating formation energies in BZO and BCO. A constant temperature of 900 K is assumed for each plot.

VBM will give rise to  $h^+$  concentrations of approximately  $2.3 \times 10^{15} \text{ cm}^{-3}$  in BZO and  $4.6 \times 10^{15} \text{ cm}^{-3}$  in BCO. This Fermi level will be reached at slightly below ambient conditions in BZO ( $P_{O_2} = 6.4 \times 10^{-2} \text{ atm}$ ), but it will require higher  $P_{O_2}$  in BCO ( $9.4 \times 10^1 \text{ atm}$ ). At ambient partial pressures ( $P_{O_2} = 10^0 \text{ atm}$ ), the  $h^+$  concentrations will be similar,  $4.5 \times 10^{15} \text{ cm}^{-3}$  in BZO (with a Fermi level of 0.95 eV above the VBM) and  $1.5 \times 10^{15} \text{ cm}^{-3}$  in BCO (with the Fermi level being 1.09 eV above the VBM).

Finally, in Fig. 5(c), we provide a concentration plot for a Ba(Zr<sub>0.5</sub>Ce<sub>0.5</sub>)O<sub>3</sub> alloy. To create this plot, we assumed that the formation energies of equivalent species ( $Y_{Zr}$  and  $Y_{Ce}$  are considered equivalent here) are the average of their formation energies in pure BZO and BCO. Similarly, the free carrier concentrations are averaged to approximate the carrier concentrations in the alloyed system. We reference the Fermi level to the VBM of BCO, and to calculate the corresponding carrier concentrations in BZO, we apply the band offset determined in Fig. 4. The trends are very similar to those in bulk materials. Concentrations for  $V_O^{+2}$  remain high, as desired, while those for free carriers are in between those of pure BCO and BZO. A Fermi level of 1 eV above the VBM can be achieved at  $P_{O_2} = 2.4 \text{ atm}$ , leading to  $h^+$  concentrations of about  $3.0 \times 10^{15} \text{ cm}^{-3}$ , while at  $P_{O_2} = 10^0 \text{ atm}$ , the  $h^+$  concentration will be about  $2.4 \times 10^{15} \text{ cm}^{-3}$ , with the Fermi level roughly 1.02 eV above the VBM.

#### IV. DISCUSSION

As seen by their absence in Fig. 5, electron concentrations will be negligibly small when BZO and BCO are doped with an acceptor species like Y. Increasing their concentrations would require Fermi levels much closer to the CBM, which in turn requires extremely O-poor conditions; such conditions will be difficult to achieve in practice, due to the need for water exposure during device operation. The low electron concentrations will correspond to low concentrations of electron polarons, as well. In pure BZO, electron polarons will not form on account of Zr's propensity as an element not to be reduced. Ce, on the other hand, can change its oxidation state relatively easily from Ce(IV) to Ce(III), giving rise to accessible electron polaron states in BCO. These states transfer directly to BZO; that is, when Ce substitutes for Zr, electrons can localize on Ce atoms within the band gap. The binding energies for these polaronic states are fairly large, suggesting that if conditions are favorable for electrons to be present, polarons will likely form. While there are some literature reports suggesting the presence of electron polarons in BCO, their concentrations are low and indeed require O-poor conditions [21,59,60].

However, hole polarons and free holes will be more prominent when the Fermi level is shifted closer to the VBM, which is a consequence of doping strategies intended to raise  $V_O^{+2}$  concentrations [7,28]. Such Fermi levels require O-rich conditions, according to Fig. 5. When used in a fuel cell, BZO and BCO are exposed to O-rich conditions near the cathode, which is directly exposed to O<sub>2</sub> gas; thus, the risk of p-type electrical conductivity is likely highest at the cathode, though it may still persist throughout the electrolyte. In an

electrolysis cell, the presence of  $\text{H}_2\text{O}$  at the cathode side may also lead to more O-rich conditions and contribute to high  $p$ -type electrical conductivity.

Literature reports have shown that hole conductivity is higher in BZO than in BCO, and that for alloys, hole conductivity decreases with increasing Ce concentration [3,21,27]. However, our results show that carrier concentrations are roughly equal in BZO and in BCO under similar conditions, meaning that concentrations alone do not explain the observed trends. One reason that hole conductivity in BZO may be higher than in BCO relates to the formation of hole polarons. As we have discussed, hole polaron binding energies in BCO are larger than those of BZO; thus, we expect a higher proportion of hole polarons relative to free carriers in BCO. The polaron binding energy rises as dilute alloy species are added to BZO:Ce and (especially) BCO:Zr, indicating a stronger preference for polaronic trapping in alloys compared to the bulk compounds. Polarons are generally far less mobile than free carriers, meaning that higher proportions of self-trapped holes should severely limit the electrical conductivity. Hole polaron mobility will be reduced for systems containing more Ce, as we found previously in the context of alloys, as polarons will be trapped by even dilute amounts of Zr.

If hole polarons are present in high concentrations, they can form complexes with acceptor species or other defects [28,29], potentially interfering with proton conduction as well as electrical conductivity. As a result, it may be worthwhile to investigate alternative dopants that introduce fewer holes and hole polarons than Y. Doing so would lead to lower  $V_{\text{O}}^{+2}$  concentrations, which per Eq. (1) are used to incorporate protons. However, one could imagine a more direct route to introducing protons into these materials that does not require  $V_{\text{O}}^{+2}$ , but rather achieves charge neutrality with  $\text{H}_i^+$  as the compensating donor species. Such an approach, potentially achieved by exposing the material directly to dry  $\text{H}_2$  during synthesis, has attracted speculation in the past [61]. At least in BZO,  $\text{H}_i^+$  has a lower formation energy than  $V_{\text{O}}^{+2}$  [7], meaning that a lower-energy acceptor dopant could achieve similar concentrations of protons via direct incorporation while requiring lower dopant concentrations, and, ergo, lower hole concentrations, than those discussed here for Y.

## V. CONCLUSION

In summary, we have investigated some of the factors contributing to electrical leakage in BZO and BCO, including from free carriers and the formation of polarons. We primarily considered the phases of BZO and BCO most stable at

ambient conditions, although we also commented on the dynamically unstable cubic BCO phase, which has relevance to BZO–BCO alloys. Hole polarons, forming on the  $2p$  orbitals of O atoms, can form in both materials, and are found to be further stabilized in the vicinity of Zr in alloys. Electron polarons form on Ce  $4f$  orbitals in BCO; however, they cannot be stabilized on Zr  $4d$  states in pure BZO, as the polaron binding energy is predicted to be less favorable than free electrons by approximately 1 eV. Alloying BZO with BCO can make electron polaron states accessible, however, as electrons can localize on Ce impurities.

In Y-doped BZO and BCO, electrons and electron polarons will form in negligibly small amounts. However, the position of the Fermi level even under standard atmospheric conditions will give rise to much higher hole concentrations. These concentrations increase for high  $\text{O}_2$  partial pressures; thus, such conditions should be avoided. The low hole polaron binding energies mean that large quantities of these free holes will likely form as polarons, particularly in BCO. The lower mobility of hole polarons compared to free holes will limit the  $p$ -type electrical conductivity, and we find that the polaron mobility will be lower in systems containing large amounts of Ce. In addition to avoiding O-rich conditions, limiting the doping levels will reduce the hole concentrations. Doing so will also limit  $V_{\text{O}}^{+2}$  concentrations; thus, it may be valuable to investigate alternative avenues for proton incorporation, which may not require such large dopant concentrations. Such efforts may be valuable for optimizing the performance of BZO–BCO alloys and related materials as proton conductors.

## ACKNOWLEDGMENTS

We acknowledge helpful discussions with K. E. Kweon, M. E. Turiansky, and C. G. Van de Walle. The authors acknowledge support from the HydroGEN Advanced Water Splitting Materials Consortium, established as part of the Energy Materials Network under the U.S. Department of Energy, the Office of Energy Efficiency and Renewable Energy (EERE), the Hydrogen and Fuel Cell Technologies Office (HFTO). Part of this work was performed under the auspices of the U.S. Department of Energy by Lawrence Livermore National Laboratory under Contract No. DE-AC52-07NA27344. M.L. additionally acknowledges support from the U.S. Department of Energy Idaho Operations Office under Contract No. DE-AC07-05ID14517. The research was performed using computational resources sponsored by the U.S. Department of Energy's EERE and located at the National Renewable Energy Laboratory.

- 
- [1] K.-D. Kreuer, *Annu. Rev. Mater. Res.* **33**, 333 (2003).
  - [2] T. Norby, *Solid State Ionics* **125**, 1 (1999).
  - [3] N. Kochetova, I. Animitsa, D. Medvedev, A. Demin, and P. Tsiakaras, *RSC Adv.* **6**, 73222 (2016).
  - [4] S. Rajendran, N. K. Thangavel, H. Ding, Y. Ding, D. Ding, and L. M. Reddy Arava, *ACS Appl. Mater. Interfaces* **12**, 38275 (2020).
  - [5] C. Y. R. Vera, H. Ding, D. Peterson, W. T. Gibbons, M. Zhou, and D. Ding, *J. Phys. Energy* **3**, 032019 (2021).
  - [6] E. Fabbri, D. Pergolesi, and E. Traversa, *Chem. Soc. Rev.* **39**, 4355 (2010).
  - [7] A. J. E. Rowberg, L. Weston, and C. G. Van de Walle, *ACS Appl. Energy Mater.* **2**, 2611 (2019).
  - [8] K. H. Ryu and S. M. Haile, *Solid State Ionics* **125**, 355 (1999).

- [9] K. Katahira, Y. Kohchi, T. Shimura, and H. Iwahara, *Solid State Ionics* **138**, 91 (2000).
- [10] J. Lü, L. Wang, L. Fan, Y. Li, L. Dai, and H. Guo, *J. Rare Earths* **26**, 505 (2008).
- [11] W. Bian, W. Wu, B. Wang, W. Tang, M. Zhou, C. Jin, H. Ding, W. Fan, Y. Dong, J. Li, and D. Ding, *Nature (London)* **604**, 479 (2022).
- [12] S. Choi, C. J. Kucharczyk, Y. Liang, X. Zhang, I. Takeuchi, H.-I. Ji, and S. M. Haile, *Nat. Energy* **3**, 202 (2018).
- [13] C.-S. Tu, R. Chien, V. H. Schmidt, S. Lee, and C. Huang, *J. Phys.: Condens. Matter* **24**, 155403 (2012).
- [14] L. Zhao, W. Tan, and Q. Zhong, *Ionics* **19**, 1745 (2013).
- [15] J. Lagaeva, D. Medvedev, A. Demin, and P. Tsiakaras, *J. Power Sources* **278**, 436 (2015).
- [16] K. Nomura and H. Kageyama, *Solid State Ionics* **178**, 661 (2007).
- [17] K. Knight, *Solid State Ionics* **74**, 109 (1994).
- [18] P. Sawant, S. Varma, B. Wani, and S. Bharadwaj, *Int. J. Hydrogen Energy* **37**, 3848 (2012).
- [19] A. J. E. Rowberg, M. W. Swift, and C. G. Van de Walle, *Phys. Chem. Chem. Phys.* **23**, 14205 (2021).
- [20] J. Exner, T. Nazareus, J. Kita, and R. Moos, *Int. J. Hydrogen Energy* **45**, 10000 (2020).
- [21] Y. Matsuzaki, Y. Tachikawa, Y. Baba, K. Sato, H. Iinuma, G. Kojo, H. Matsuo, J. Otomo, H. Matsumoto, S. Taniguchi, and K. Sasaki, *ECS Trans.* **91**, 1009 (2019).
- [22] T. Nakamura, S. Mizunuma, Y. Kimura, Y. Mikami, K. Yamauchi, T. Kuroha, N. Taniguchi, Y. Tsuji, Y. Okuyama, and K. Amezawa, *J. Mater. Chem. A* **6**, 15771 (2018).
- [23] T. Somekawa, Y. Matsuzaki, M. Sugahara, Y. Tachikawa, H. Matsumoto, S. Taniguchi, and K. Sasaki, *Int. J. Hydrogen Energy* **42**, 16722 (2017).
- [24] A. Grimaud, J. Bassat, F. Mauvy, P. Simon, A. Canizares, B. Rousseau, M. Marrony, and J. Grenier, *Solid State Ionics* **191**, 24 (2011).
- [25] F. Iguchi, T. Tokikawa, T. Miyoshi, T. Tsurui, Y. Nagao, N. Sata, and H. Yugami, *ECS Trans.* **7**, 2331 (2007).
- [26] A. Kuz'min, V. Balakireva, S. Plaksin, and V. Gorelov, *Russian J. Electrochem.* **45**, 1351 (2009).
- [27] D. Han, X. Liu, T. S. Bjørheim, and T. Uda, *Adv. Energy Mater.* **11**, 2003149 (2021).
- [28] M. W. Swift, A. Janotti, and C. G. Van de Walle, *Phys. Rev. B* **92**, 214114 (2015).
- [29] A. Lindman, P. Erhart, and G. Wahnström, *Phys. Rev. B* **94**, 075204 (2016).
- [30] J. M. Polfus, M. Pishahang, and R. Bredesen, *Phys. Chem. Chem. Phys.* **20**, 16209 (2018).
- [31] P. Liao, M. C. Toroker, and E. A. Carter, *Nano Lett.* **11**, 1775 (2011).
- [32] J. J. Carey and K. P. McKenna, *J. Phys. Chem. C* **123**, 22358 (2019).
- [33] W. Kohn and L. J. Sham, *Phys. Rev.* **140**, A1133 (1965).
- [34] P. Hohenberg and W. Kohn, *Phys. Rev.* **136**, B864 (1964).
- [35] G. Kresse and J. Furthmüller, *Phys. Rev. B* **54**, 11169 (1996).
- [36] G. E. Heyd, J. Scuseria, and M. Ernzerhof, *J. Chem. Phys.* **124**, 219906 (2006).
- [37] D. Vignesh and E. Rout, *Comput. Condens. Matter* **33**, e00763 (2022).
- [38] P. E. Blöchl, *Phys. Rev. B* **50**, 17953 (1994).
- [39] G. Kresse and D. Joubert, *Phys. Rev. B* **59**, 1758 (1999).
- [40] R. Borja-Urby, L. A. Diaz-Torres, P. Salas, M. Vega-Gonzalez, and C. Angeles-Chavez, *Mater. Sci. Eng. B* **174**, 169 (2010).
- [41] M. Huntelaar, A. Booiij, and E. Cordfunke, *J. Chem. Thermodyn.* **26**, 1095 (1994).
- [42] O. Fursenko, J. Bauer, G. Lupina, P. Dudek, M. Lukosius, C. Wenger, and P. Zaumseil, *Thin Solid Films* **520**, 4532 (2012).
- [43] E. Cordfunke, A. Booiij, and M. Huntelaar, *J. Chem. Thermodyn.* **30**, 437 (1998).
- [44] T. He, P. Ehrhart, and P. Meuffels, *J. Appl. Phys.* **79**, 3219 (1996).
- [45] C. Freysoldt, B. Grabowski, T. Hickel, J. Neugebauer, G. Kresse, A. Janotti, and C. G. Van de Walle, *Rev. Mod. Phys.* **86**, 253 (2014).
- [46] C. Freysoldt, J. Neugebauer, and C. G. Van de Walle, *Phys. Rev. Lett.* **102**, 016402 (2009).
- [47] C. Freysoldt, J. Neugebauer, and C. G. Van de Walle, *Phys. Status Solidi B* **248**, 1067 (2011).
- [48] M. W. Chase Jr., *J. Phys. Chem. Ref. Data*, Monograph **9**, 1 (1998).
- [49] B. J. Van Zeghbroeck, *Principles of Semiconductor Devices* (University of Colorado Press, Boulder, 2011).
- [50] M. Aycibin, B. Erdinc, and H. Akkus, *J. Electronic Mater.* **43**, 4301 (2014).
- [51] H. Fröhlich, *Adv. Phys.* **3**, 325 (1954).
- [52] A. Jain, S. P. Ong, G. Hautier, W. Chen, W. D. Richards, S. Dacek, S. Cholia, D. Gunter, D. Skinner, G. Ceder, and K. A. Persson, *APL Mater.* **1**, 011002 (2013).
- [53] K. Momma and F. Izumi, *J. Appl. Crystallogr.* **44**, 1272 (2011).
- [54] B. Sadigh, P. Erhart, and D. Åberg, *Phys. Rev. B* **92**, 075202 (2015).
- [55] M. Peressi, N. Binggeli, and A. Baldereschi, *J. Phys. D: Appl. Phys.* **31**, 1273 (1998).
- [56] J. Tersoff, *Phys. Rev. B* **30**, 4874 (1984).
- [57] L. Weston, H. Taylor, K. Krishnaswamy, L. Bjaalie, and C. Van de Walle, *Comput. Mater. Sci.* **151**, 174 (2018).
- [58] P. G. Sundell, M. E. Björketun, and G. Wahnström, *Phys. Rev. B* **73**, 104112 (2006).
- [59] P. Pulphol, N. Vittayakorn, W. Vittayakorn, and T. Kolodiaznyi, *Appl. Phys. A* **125**, 197 (2019).
- [60] F. J. Loureiro, D. Pérez-Coll, V. C. Graça, S. M. Mikhalev, A. F. Ribeiro, A. Mendes, and D. P. Fagg, *J. Mater. Chem. A* **7**, 18135 (2019).
- [61] T. Norby, M. Widerøe, R. Glöckner, and Y. Larring, *Dalton Trans.* **19**, 3012 (2004).